PNAS RESEARCH ARTICLE | EARTH, ATMOSPHERIC, AND PLANETARY SCIENCES
ENVIRONMENTAL SCIENCES

Extreme accumulation of ammonia on electroreduced mackinawite: An abiotic ammonia storage mechanism in early ocean hydrothermal systems

Wataru Takahagi[a,b,c,1], Satoshi Okada[b,1], Yohei Matsui[d], Shigeaki Ono[e], Ken Takai[b], Yoshio Takahashi[f], and Norio Kitadai[b,g,1]

Edited by Micheal J. Russell, NASA Exoplanet Science Institute, Rho, Italy; received February 26, 2023; accepted August 14, 2023, by Editorial Board Member Donald E. Canfield

An increasing amount of evidence suggests that early ocean hydrothermal systems were sustained sources of ammonia, an essential nitrogen species for prebiotic synthesis of life's building blocks. However, it remains a riddle how the abiotically generated ammonia was retained at the vent–ocean interface for the subsequent chemical evolution. Here, we demonstrate that, under simulated geoelectrochemical conditions in early ocean hydrothermal systems (≤ -0.6 V versus the standard hydrogen electrode), mackinawite gradually reduces to zero-valent iron (Fe^0), generating interlayer Fe^0 sites. This reductive conversion leads to an up to 55-fold increase in the solid/liquid partition coefficient for ammonia, enabling over 90% adsorption of 1 mM ammonia in 1 M NaCl at neutral pH. A coordinative binding of ammonia on the interlayer Fe^0 sites was computed to be the major mechanism of selective ammonia adsorption. Mackinawite is a ubiquitous sulfide precipitate in submarine hydrothermal systems. Given its reported catalytic function in amination, the extreme accumulation of ammonia on electroreduced mackinawite should have been a crucial initial step for prebiotic nitrogen assimilation, paving the way to the origin of life.

astrobiology | life emergence | prebiotic chemistry | geochemistry

Significance

Life on Earth has long been suggested to have originated in submarine hydrothermal systems. Although this hypothesis has been investigated by numerous prebiotic experiments, it remains a conundrum what geochemical mechanism led to accumulation of ammonia, an essential nitrogen species for abiotic synthesis of life's building blocks. Here, we show that mackinawite, an iron sulfide mineral common in submarine hydrothermal systems, drastically enhances its adsorption capability for ammonia through electroreduction to zero-valent iron, enabling over 90% accumulation of 1 mM ammonia in 1 M NaCl at neutral pH. Given spontaneous generation of electricity widespread in present ocean hydrothermal vent environments, our demonstrated electrochemical mechanism of ammonia accumulation is likely to have been a ubiquitous geochemical phenomenon on the early seafloor.

It has long been suggested that submarine hydrothermal systems were among the most suitable settings for the origin and early evolution of life (1–3). Supporting this hypothesis are laboratory simulations demonstrating abiotic synthesis of ammonia/ammonium ion (NH_3/NH_4^+; hereafter referred to simply as ammonia), an essential nitrogen species for the production of the building blocks of life. To date, a variety of iron-bearing minerals seen in hydrothermal vent environments, such as iron sulfides (4–6), magnetite (5), komatiite (7), green rust (8), and iron–nickel alloys (9), has been shown to facilitate ammonia formation via the reduction of nitrate (NO_3^-) and nitrite (NO_2^-) in water. Efficient nitrate and nitrite reductions to ammonia have also been demonstrated on molybdenum sulfide (MoS_2) as an electrocatalyst (10, 11). Based on these results, along with experimental and computational estimates on the production rates of nitrate and nitrite through atmospheric/oceanic processes (12), micro- to submillimolar concentrations of ammonia have been suggested to be supplied sustainably at the vent–ocean interface of early ocean hydrothermal systems (7).

However, it remains a question as to how the abiotically generated ammonia was retained and accumulated within vent chimneys for the subsequent chemical evolution of life. Laboratory simulations of prebiotic organic synthesis typically use 100 mM or higher concentrations of ammonia (13). To the best of our knowledge, 5 mM is the reported lowest concentration of ammonia used for the synthesis of amino acids (14); however, in the presence of 5 mM ammonia, the yields of glycine and alanine from corresponding keto acids (2.5 mM) were as low as 1.1% and 0.36%, respectively (28 and 9 μM, respectively). In the early ocean, the steady-state concentration of ammonia has been estimated to be 3.6–70 μM (15), which is four to five orders of magnitude lower than that of the major seawater cation, Na^+ (1 M) (16). Given the neutral or monocationic nature of ammonia, its weak electrostatic interaction with negatively charged mineral surfaces is unlikely to suppress the diffusive loss of ammonia into seawater. Certain clay minerals (e.g., kaolinite, montmorillonite, and vermiculite) and zeolites are known to selectively adsorb ammonia in their interlayer and/or nanopore structures (17–20). However, their availability on the early ocean floor is unclear (21, 22).

Here, we report the exceptional capability of mackinawite (FeS), an iron sulfide mineral ubiquitous in submarine hydrothermal systems, for ammonia accumulation triggered by electrochemical reduction. A recent in situ electrochemical survey of the Okinawa Trough

The authors declare no competing interest.

This article is a PNAS Direct Submission. M.J.R. is a guest editor invited by the Editorial Board.

[1]To whom correspondence may be addressed. Email: watarut@g.ecc.u-tokyo.ac.jp, okadasa@jamstec.go.jp, or nkitadai@jamstec.go.jp.

This article contains supporting information online at https://www.pnas.org/lookup/suppl/doi:10.1073/pnas.2303302120/-/DCSupplemental.

Published October 2, 2023.

hydrothermal fields revealed that spontaneous generation of electricity is widespread in deep-sea vent chimneys and mineral deposits (23, 24). Subsequent laboratory simulations of the geoelectrochemical system have demonstrated (electro)catalytic functions of metal sulfides for organic/inorganic reactions crucial for the origin of life (25–29). Furthermore, it was found that under a negative electric potential realizable in early ocean hydrothermal systems, certain metal sulfides, including mackinawite, undergo hour- to day-scale electroreduction to corresponding metals, thereby drastically enhancing their capabilities of promoting prebiotically important reactions (30, 31).

Mackinawite has a layered crystalline structure with an interlayer distance of 0.5 nm (32). Because the intralayer Fe–Fe distance (0.260 nm)(32) is close to the molecular diameter of NH_3 (0.26 nm)(33), the detachment of sulfur atoms through mackinawite electroreduction to zero-valent iron ($FeS + 2H^+ + 2e^- \longrightarrow Fe^0 + H_2S$) is expected to form angstrom-size pores on the interlayer surface, within which ammonia may stably coordinate to the exposed Fe^0 site. Our experiment shown below demonstrates a drastic increase in the ammonia adsorption onto mackinawite through its electroreduction.

Notice that our unveiled electrochemical mechanism leading to ammonia accumulation is different from that developed for ammonia removal from wastewaters (34, 35). In the wastewater treatment, an electrochemically generated pH gap between two compartments, separated by a hydrophobic membrane, has been utilized to induce a spontaneous ammonia transfer from the anode to the cathode. Importantly, mackinawite is not a mere ammonia adsorbent. Considering the catalytic function of pure and electroreduced mackinawite in the amination reaction (30, 36, 37), mackinawite is likely to have served as an entry point for nitrogen into prebiotic chemistry, leading to the formation of N-containing building blocks of life.

Results

Ammonia Adsorption onto Electroreduced Mackinawite. Mackinawite was prepared by simply mixing an aqueous solution of iron chloride ($FeCl_2$) and sodium sulfide (Na_2S). The obtained mackinawite (300 mg) was immersed in 1 M NaCl containing 1 mM NH_4Cl (60 mL) and exposed to a constant electric potential for 48 h at room temperature (25 ± 2 °C) using an H-type cell (*SI Appendix*, Fig. S1). The solution pH was maintained at slightly acidic to neutral (6.3 ± 1.2; *SI Appendix*, Fig. S2) by continuous CO_2 bubbling (20 $mLmin^{-1}$). In the course of mackinawite electrolysis, the supernatant solution was sampled periodically (1 mL for each) and measured for the dissolved ammonia concentration through high-performance liquid chromatography (HPLC). The quantified concentration was used to calculate the amount of ammonia adsorption onto mackinawite, assuming ammonia partitioning between the liquid and adsorbed phases. After the electrolysis, mackinawite was separated from the supernatant solution, dried under vacuum, and characterized with the techniques described below and in *SI Appendix*.

Fig. 1*A* shows the X-ray diffraction (XRD) patterns of mackinawite after the 48-h experiment. Consistent with our previous observation (30, 31), mackinawite electrolyzed at $\leq -0.6V_{SHE}$ (versus the standard hydrogen electrode) exhibited a broad but recognizable XRD signal at 44.7°, which is assigned to the α-form of Fe^0 with a body-centered cubic structure (Fig. 1*A*). The formation of Fe^0 was also indicated by energy-dispersive X-ray spectroscopy (EDS) on the electrolyzed mackinawite, in which a clear decrease in the sulfur signal intensity relative to iron was observed in comparison with nonelectrolyzed mackinawite (Fig. 1*B* and *SI Appendix*, Fig. S3; EDS data in Fig. 1*B* are normalized by S K line signal at 2.31 keV.). The Fe/S intensity ratio reflects the degree of $FeS - to - Fe^0$ electroreduction (Fig. 1*C* and *SI Appendix*, Table S1). It was estimated that the percentage of Fe^0 in electrolyzed mackinawite remained approximately zero at −0.2 and −0.5 V_{SHE}, turned positive at $-0.6V_{SHE}$, and increased at lower potentials to 18 ± 1.7% at $-1.0V_{SHE}$, in agreement with thermodynamic calculations (30, 31). The occurrence and growth of Fe^0 was furthermore suggested by ex-situ measurements of the iron K-edge extended X-ray absorption fine structure (EXAFS) (*SI Appendix*, Fig. S4). At $-0.9V_{SHE}$, longer reaction duration led to greater spectral distortion particularly in the wavenumber range from 9 to 11 $Å^{-1}$. A least-squares fitting of the sample EXAFS spectra with those of pure FeS and pure Fe^0 revealed an increase in the percentage of Fe^0 for the initial 24 h up to around 5% (*SI Appendix*, Figs. S4*D* and S5). The estimated percentage after the 48-h electrolysis is lower than that determined by EDS (14.5 ± 1.7%; Fig. 1*C*) possibly because of the attenuated amplitude of EXAFS oscillation in k space due to the particle size of Fe^0; smaller particles in several-nm scale tend to exhibit lower EXAFS oscillation in the k space spectra (38, 39). Thus, although the EXAFS data support the conversion of FeS to Fe^0, the EDS-determined percentages of Fe^0 (Fig. 1*C*) are more reliable and hence, will be used in the following discussion. Considering the observation that the concentration of Fe^{2+} in supernatant solution was suppressed by applying a potential of $\leq -0.6V_{SHE}$ (*SI Appendix*, Fig. S6), the $FeS - to - Fe^0$ electroreduction likely proceeded via the dissolution of Fe^{2+} and its subsequent electrodeposition. The dissolution/precipitation mechanism is supported by the decrease in the Brunauer–Emmett–Teller specific surface area (SSA_{BET}) of mackinawite, particularly at $\leq -0.6V_{SHE}$ (Fig. 1*D* and *SI Appendix*, Figs. S7 and S8). No appearance of an XRD signal for Fe^0 at the threshold potential ($-0.6V_{SHE}$; Fig. 1*A*) suggests that Fe^0 atoms were atomically dispersed in the mackinawite structure. Such dispersing Fe^0 may serve as seeds for the crystal growth of α-Fe^0 at lower potentials.

At $-0.5V_{SHE}$, the concentration of Fe^{2+} in supernatant solution was also suppressed (*SI Appendix*, Fig. S6). Although $-0.5V_{SHE}$ is insufficient for the $FeS - to - Fe^0$ electroreduction (Fig. 1 *A*–*C*), a weak current was observed during the experiment due to H_2 evolution ($2H^+ + 2e^- \rightarrow H_2$; Eh = $-0.36V_{SHE}$ at pH 6) (*SI Appendix*, Fig. S9). This H^+-to-H_2 conversion is expected to increase the surface pH of mackinawite, suppressing the dissolution of Fe^2+ ($FeS + 2H^+ \rightarrow Fe^2 + +H_2S$).

The concentration of dissolved ammonia also varied significantly with applied potential (Fig. 2*A*). Compared with the result in the absence of an applied potential, which showed a 11 ± 0.24% decrease after the 48-h experiment, no appreciable influence of the $-0.2V_{SHE}$ exposure was discerned, whereas greater and steeper decreases occurred at lower potentials. The lowest concentration of 0.056 mM was observed at −0.8 and $-0.9V_{SHE}$ after the 48-h experiment, which corresponds to 171 $\mu mol\ g^{-1}$ of ammonia adsorption onto mackinawite (Fig. 2, *b-1*) and a solid/liquid partition coefficient of 1.2 Lg^{-1} (Fig. 2, *b-2*). As the SSA_{BET} of mackinawite decreased substantially at $\leq -0.6V_{SHE}$ (Fig. 1*D*), the SSA_{BET}-based adsorption amount of ammonia reached 72.4 molecules nm^{-2} at $-0.9V_{SHE}$, which was approximately 600 times higher than that in the absence

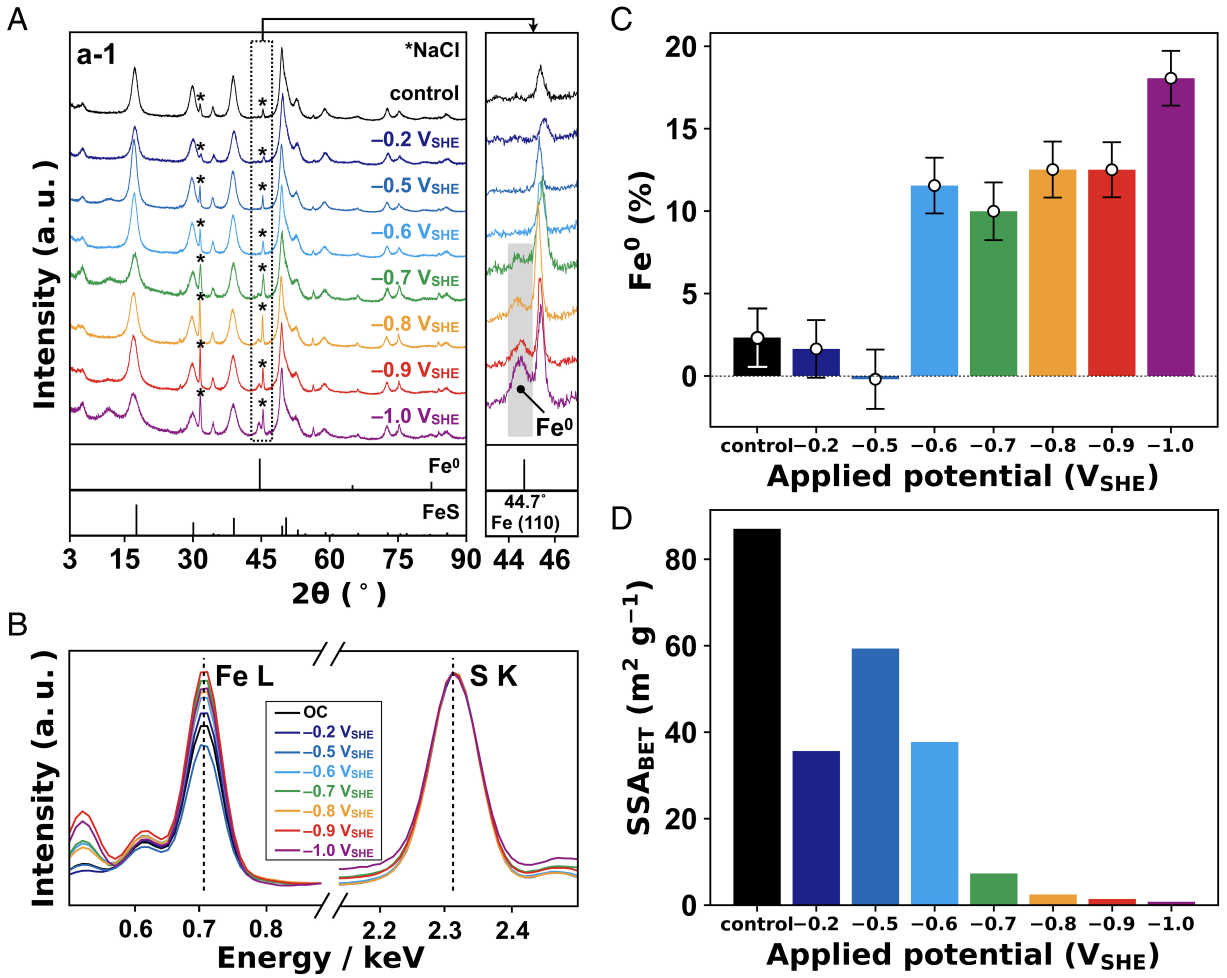

Fig. 1. Characteristics of electrolyzed mackinawite. (*A*) XRD patterns of mackinawite. Asterisks show the residual NaCl, and spectra at 43–47° are magnified on the right. The condition without applying voltage is shown as control. (*B*) Normalized EDS spectra. EDS profiles in a wider energy range (0–4 keV) are shown in *SI Appendix*, Fig. S3. (*C*) Percentages of Fe^0 in electrolyzed mackinawite determined from the EDS signal intensity of Fe (0.7 keV) relative to S (2.3 keV). Error bars are the SD of EDS measurements. (*D*) BET-specific surface area. We did not carry out the electrochemical experiment at potentials between $-0.2V_{SHE}$ and $-0.5V_{SHE}$ because the potential monitored during the control experiment ranged between $-0.3V_{SHE}$ and $-0.4V_{SHE}$ (*SI Appendix*, Fig. S10).

of an applied potential (0.12 molecules nm^{-2}) (Fig. 2, *b-3*). In units of "molecules nm^{-2}," the surface density of ammonia adsorption at $-1.0V_{SHE}$ was similar to that at $-0.9V_{SHE}$ (Fig. 2, *b-3*), although the mass-based adsorption value (μmol g^{-1}) at $-1.0V_{SHE}$ was 48% lower than that at $-0.9V_{SHE}$ (Fig. 2, *b-1*). At $-1.0V_{SHE}$, the SSA_{BET} of mackinawite decreased to 0.79 m^2g^{-1}, whereas that after the $-0.9V_{SHE}$ electrolysis was 1.42 m^2g^{-1} (Fig. 1*D* and *SI Appendix*, Table S2). This greater decrease in SSA_{BET} at lower potential is the cause of the apparent discrepancy. The adsorbed ammonia was also characterized with an elemental analyzer/isotope ratio mass spectrometer (EA/IRMS). The longer the duration of FeS electrolysis at $-0.9V_{SHE}$, the more nitrogen (N) was released from the electrolyzed FeS through combustion (*SI Appendix*, Fig. S11). The amounts of N per gram of FeS samples (μmol g^{-1}) were slightly lower than the adsorption amounts of ammonia determined from the dissolved ammonia concentrations (Fig. 2 *A* and *B*) probably because of partial desorption of ammonia through the vacuum drying of FeS samples (*Materials and Methods*).

After the electrolysis, the ammonia accumulated on electrolyzed mackinawite was mostly retained over several hours (*SI Appendix*, Fig. S12). Subsequent monitoring without an externally imposed electric potential found a gradual desorption of ammonia, together with an increase in the open-circuit potential (OCP). The increase in OCP is ascribed to the oxidation of Fe^0 to siderite ($Fe^0 + CO_2 + H_2O \longrightarrow FeCO_3 + H_2$), as indicated by the XRD pattern presented in *SI Appendix*, Fig. S13.

Importance of the Interlayer Fe^0 Sites for Ammonia Accumulation. What surface mechanism was responsible for the drastic increase in ammonia adsorption onto mackinawite at $\leq -0.6V_{SHE}$? SSA_{BET}-based adsorption attained at $-0.9V_{SHE}$ (72.4 molecules nm^{-2}; Fig. 2, *b-3*) is far greater than the density of surface sites for ion adsorption onto mackinawite (>FeSH; 4.0 sites nm^{-2}) (40). Thus, a well-known electrostatic ion–surface interaction is not a major mechanism leading to ammonia accumulation. During the electrolysis, the vicinity of the mackinawite surface is expected to become alkaline owing to H_2 evolution ($2H^+ + 2e^- \longrightarrow H_2$) (27). However, a batch adsorption experiment without an applied potential showed, at most, a twofold increase in the ammonia adsorption by solution alkalization (pH 10 was the optimum condition; *SI Appendix*, Fig. S14), indicating a minor contribution of surface alkaline pH.

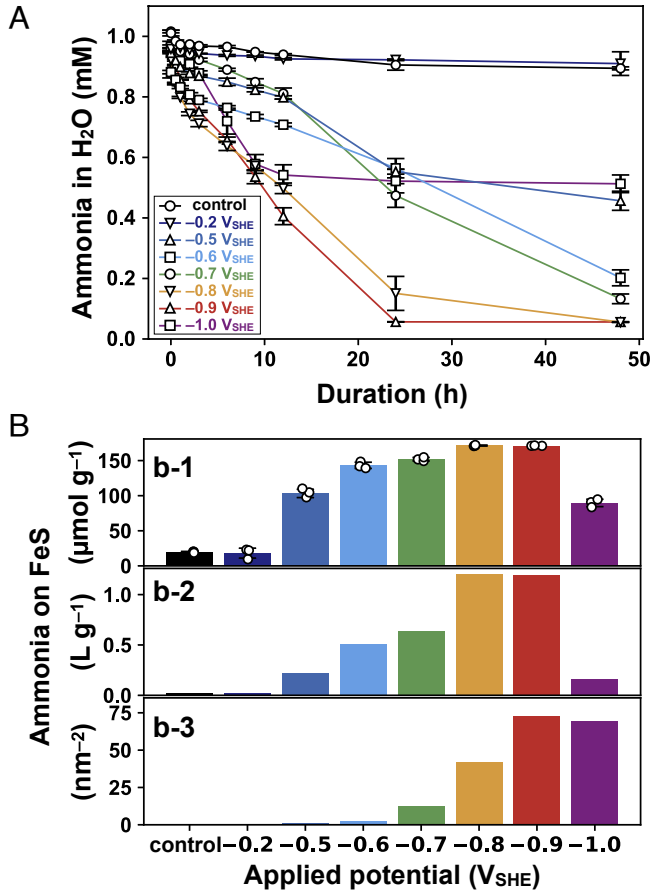

Fig. 2. Ammonia adsorption onto electrolyzed mackinawite. (*A*) Changes in the dissolved concentration of ammonia during mackinawite electrolysis. Error bars represent the SE of three independent experiments. (*B*) Mass- and SSA_{BET}-based adsorption value of ammonia on mackinawite after the 48-h electrolysis (*b-1* and *b-3*, respectively). The solid/liquid partition coefficient is also shown in *b-2*.

In light of the reported high affinity of NH_3 to pure Fe^0 (41, 42), an alternative interpretation is that the electroreduced mackinawite accumulated ammonia on the interlayer Fe^0 sites through the coordinative binding of NH_3. The Fe atoms in mackinawite are oriented in a square planar geometry with an Fe–Fe distance of 0.26 nm, constituting the (001) plane (Fig. 3*A*) (32, 40). Our first-principles calculations (*SI Appendix*, Tables S3–S14) revealed that the removal of one sulfur atom from the 4×4×1 supercell (corresponding to a 6.25% conversion of FeS to Fe^0) resulted in the shrinkage of intra- and intersheet Fe-Fe distances from 2.53/5.02 Å to 2.40/4.98 Å, respectively. When structure optimization was performed with an intercalated NH_3 molecule, the energetically most favorable position of NH_3 was confirmed to be on the exposed Fe site (Fig. 3*B* and *SI Appendix*, Table S15). The intercalation of NH_3 distorted the crystal symmetry around the active Fe site from tetragonal to triclinic, elongating the intra- and intersheet Fe–Fe distances toward the original values (2.48–2.60 and 5.05 Å, respectively). The calculated shortest distance between Fe and N (2.00 Å) corresponded well with the sum of their covalent radii (2.03 Å, where Fe is in the low spin state) (43), indicating the covalent character of the Fe–N bond. The overall energy associated with NH_3 intercalation was −1.34eV, whereas that in pure mackinawite was +0.63eV. Thus, spontaneous intercalation of NH_3 requires FeS − to − Fe^0 electroreduction.

Consistent with our interpretation, other iron-containing minerals, such as hematite, magnetite, and ferrihydrite, adsorbed greater amounts of ammonia when they were partially electroreduced to Fe^0 (*SI Appendix*, Figs. S15–S17). Note, however, that on these minerals, only surface-exposing Fe atoms are available for the NH_3 binding. In contrast, each Fe atom in mackinawite belongs to the interlayer and, thus, potentially serves as the binding site for NH_3. In the SSA_{BET} measurement, the interlayer surface is invisible, owing to the persistence of intercalated H_2O, even after vacuum drying (32). As a consequence, electrolyzed mackinawite adsorbed even greater amounts of ammonia than did pure Fe^0 under identical electrochemical conditions. At $-0.9V_{SHE}$, for example, pure Fe^0 nanoparticles (95–105 nm, >99.5% purity) adsorbed ammonia at the SSA_{BET}-based adsorption amount of 7.4 molecules nm^{-2} (*SI Appendix*, Fig. S15). Given the molecular size of NH_3 (0.26 nm in diameter) (33), the observed surface density is close to the saturation level of monolayer NH_3 adsorption. In contrast, the 72.4 molecules nm^{-2} attained by mackinawite at $-0.9V_{SHE}$ (Fig. 2, *b-3*) corresponds to 1.4 atom% of Fe in its structure, which is lower than the amount of Fe^0 generated at this potential (15 ± 1.7%; Fig. 1*C*). Thus, even denser ammonia adsorption is expected to be achieved if the experiment is performed with higher initial concentrations of ammonia.

Interestingly, in the case when mackinawite was electrolyzed at $-0.9V_{SHE}$ for 48 h in the absence of dissolved ammonia, after which ammonia was added in the supernatant solution to a concentration of 1 mM, ammonia was found to be largely retained in the liquid phase over the subsequent 48 h under the imposed potential (*SI Appendix*, Fig. S18). Mackinawite electroreduction possibly causes the aggregation of Fe sheets through Fe^0 formation and crystallization, after which NH_3 intercalation may be structurally difficult. This inhibitive effect of excessive electroreduction is also suggested in the evolution of dissolved ammonia concentration presented in Fig. 2*A*. At the lowest examined potential ($-1.0V_{SHE}$), the decrease in dissolved ammonia concentration ceased in the first 12 h, possibly because of a rapid aggregation of mackinawite Fe sheets; meanwhile, a slow Fe^0 formation at moderately negative potentials (−0.6 and $-0.7V_{SHE}$) allowed continuous ammonia accumulation over 48 h. Thus, extremely low electric potential (e.g., $-1.0V_{SHE}$) is not necessarily preferable; the potentials slightly below the FeS/Fe^0 equilibrium (e.g., $-0.6V_{SHE}$) are rather advantageous to maintaining the ammonia accumulation on mackinawite for a long duration.

Discussion

The origin of life in deep-sea hydrothermal systems is a long-standing hypothesis supported by diverse scientific disciplines, including geology (44), biology (45), and astronomy (46). However, its chemical plausibility remains a question because of the apparent difficulty in the retention and accumulation of key prebiotic components. Here, we demonstrated that partial electroreduction of mackinawite drastically enhances its ammonia accumulation capability, by up to 55-fold for the solid/liquid partition coefficient, enabling over 90% adsorption of 1 mM ammonia in 1 M NaCl at neutral pH (Fig. 2*B*). The electrochemical conditions favorable for this process are fully compatible with those suitable for prebiotic carbon and nitrogen fixations in the formation of the building blocks of life (10, 11, 25–31) (Fig. 4). The threshold potential ($-0.6V_{SHE}$) corresponds to the H^+/H_2 redox potential in a moderately

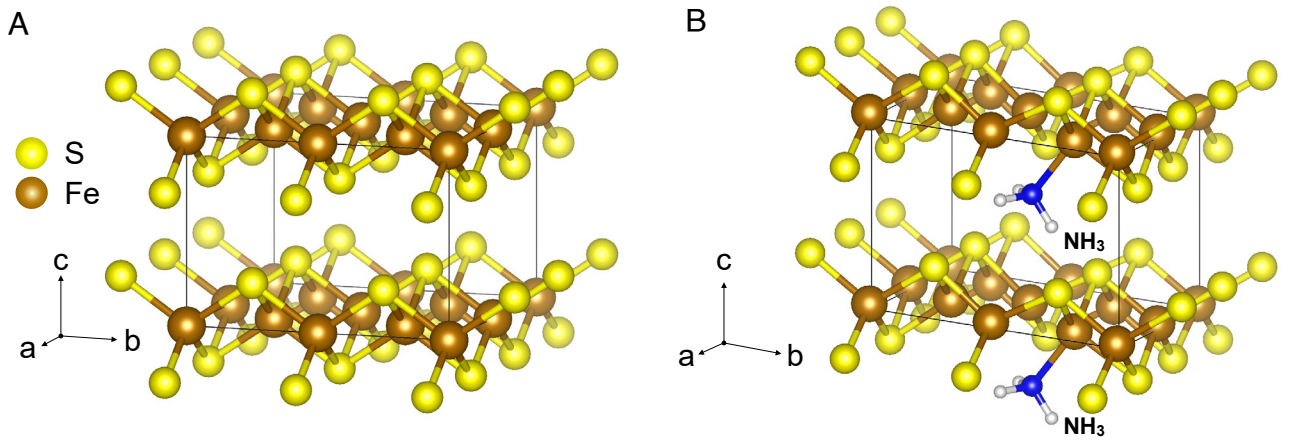

Fig. 3. Supercell (2×2×1) structures of (*A*) pure and (*B*) electrolyzed mackinawite computed by first-principles calculations. In *B*, the FeS – to – Fe^0 electroreduction is expressed by the removal of one S atom from the interlayer surface. The resultant surface-exposed Fe was found to be the energetically most favorable site for the NH_3 intercalation (see text).

alkaline, high-temperature hydrothermal environment [e.g., pH 8.7 at 100 °C in the presence of 1 mM H_2(27)], which is available even in present-day alkaline hydrothermal systems (47, 48). Although modern ocean alkaline hydrothermal vents are mainly composed of carbonate minerals that are electrochemically nonconductive (49), the early counterparts were sulfide-rich, owing to the presence of metal-rich seawater (50).

Iron sulfide must have been a predominant sulfide component of the ancient vent chimneys (51). Its catalytic surface with metal impurities (e.g., Ni^{2+}) facilitates both the oxidation of H_2 ($H_2 \longrightarrow 2H^+ + 2e^-$) and the reduction of oxidative chemicals (e.g., $CO_2 + H^+ + 2e^- \longrightarrow HCOO^-$) (29); hence, a sustained electron flow across the potential gap between the reductive hydrothermal fluid and seawater has been envisioned (Fig. 4). Pure and electroreduced mackinawite is also capable of facilitating ammonia formation (30) and promotes the amination reaction when a sufficient concentration of ammonia is available (30, 37). These facts, along with our demonstrated extreme accumulation of ammonia on electroreduced mackinawite, suggest that mackinawite played a pivotal role in the formation,

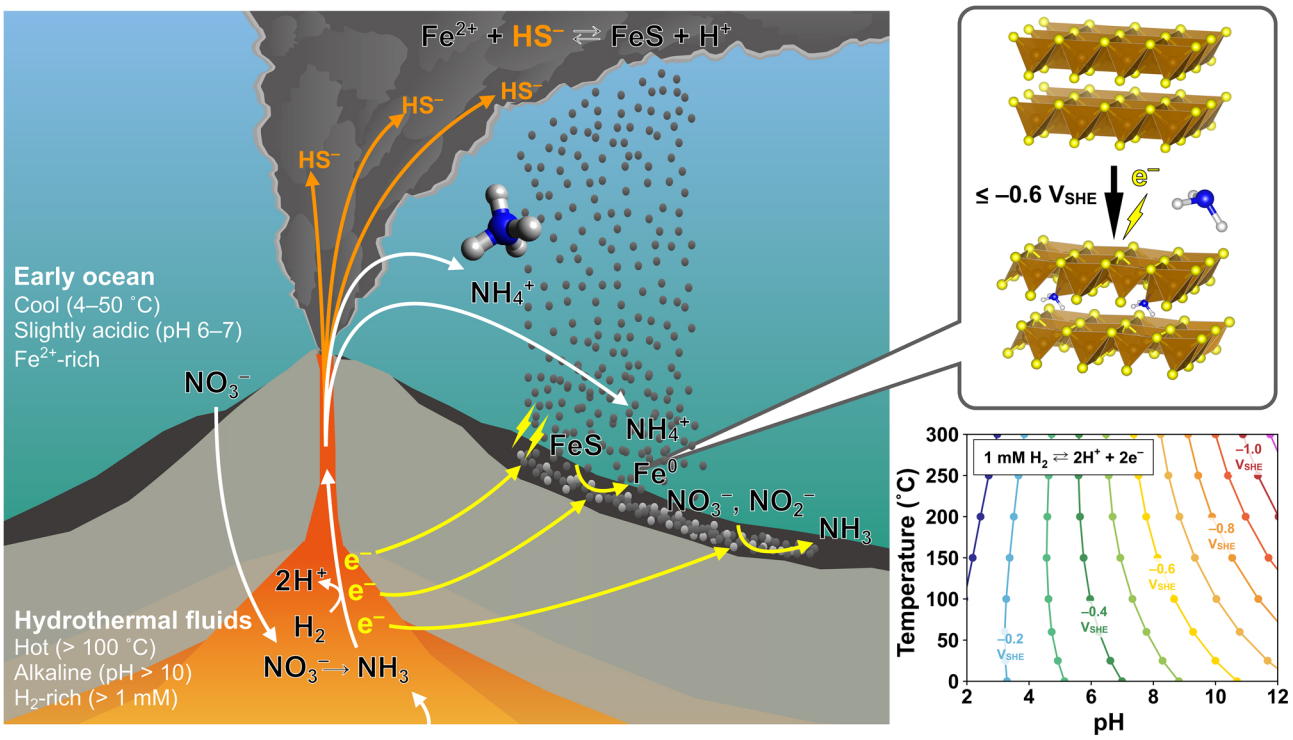

Fig. 4. Geoelectrochemical mechanism of ammonia accumulation in the early ocean hydrothermal system. The schematic was depicted based on our experimental results together with the field and laboratory findings on the geoelectrochemical processes in submarine hydrothermal systems reported in the literature (10, 11, 23, 24, 29, 30). Thermodynamic calculations for the H^+/H_2 redox potential as a function of pH and temperature (31) (*Right*) indicate that the electric potential necessary for the FeS – to – Fe^0 reduction and the subsequent NH_3 accumulation ($\leq -0.6 V_{SHE}$) is readily realizable in H_2-rich, alkaline hydrothermal systems that were ubiquitous on the early ocean floor (51).

accumulation, and assimilation of organic compounds of ammonia in the early ocean hydrothermal vent environments. Submarine hydrothermal systems are currently the sole environment in which spontaneous electricity generation has been observed (24), thus possessing a crucial advantage in abiotic nitrogen assimilation, a requisite step for the originating of life.

Materials and Methods

Preparation of Mineral Adsorbents. All chemicals were reagent grade, purchased from either Nacalai Tesque Inc., Kanto Chemical Co., Ltd., or Fujifilm Wako Pure Chemical Co., Ltd., except for pure Fe^0 nanoparticle (95–105 nm, >99.5% purity), which was obtained from EM Japan. Deaerated Milli-Q water (18.2 megohms) was used as the solvent. Mineral adsorbents were prepared, in an anaerobic chamber filled with N_2 and H_2 gases (volume ratio = 96:4).

Mackinawite was prepared by adding 100 mM Na_2S dropwise into 100 mM $FeCl_2$ under vigorous stirring to a final volume ratio of 1:1. The obtained precipitate was separated from the supernatant solution by centrifugation (8,000 rpm, 10 min) and dried under vacuum.

For the preparation of hematite, 50 mL of 0.2 M $FeCl_3$ was added dropwise into 450 mL of a boiled HCl solution (2 mM) under vigorous stirring (52, 53). The obtained suspension was inserted into a polytetrafluoroethylene (PTFE) bottle, enclosed in a screw-capped stainless-steel outer vessel, and heated at 98 °C for 14 d. After the vessel was cooled to room temperature, the resultant precipitate was rinsed with Milli-Q water, centrifuged (6,000 rpm, 10 min), and dried under vacuum.

For magnetite preparation, 19 mmol of $FeCl_3.6H_2O$ and 10 mmol of $FeCl_2.4H_2O$ were dissolved in 25.85 mL of 0.39 M HCl. The acid mixture was added dropwise into 250 mL of 1.5 M NaOH under vigorous stirring (54). The obtained black precipitate was separated from the supernatant solution by centrifugation (6,000 rpm, 10 min), dried under vacuum, and grounded with an agate mill.

For ferrihydrite preparation, 50 mM $FeCl_3$ was basified to pH 8.0 with 0.1 or 1 M NaOH and stirred over 3 h at a pH maintained at 8 (55). The obtained precipitate was separated from the supernatant solution by centrifugation (6,000 rpm, 10 min), rinsed with Milli-Q water, and dried under vacuum.

Electrochemical Experiments. Electrochemical experiments were conducted under simulated early ocean conditions in accordance with the procedure reported previously (27, 30, 31). Briefly, 300 mg of solid adsorbent was deposited on a carbon working electrode (5.7 cm^2) in an H-type cell (*SI Appendix*, Fig. S1), immersed in a deaerated 1 M NaCl containing 1 mM NH_4Cl (60 mL), and exposed to a flow of CO_2 (20 mL min^{-1}, purity > 99.995%) to maintain the solution pH at neutral (6.3 ± 1.2; *SI Appendix*, Fig. S2). Although the experimental pressure (1 atm) is lower than the pressure in deep-sea environments, this parameter has no significant influence on the FeS/Fe^0 redox potential (30).

As the CO_2 gas flow that was started at least 1 h before each experiment was maintained, a constant potential was applied on the carbon electrode for 48 h by using a multipotentiostat (PS-08; Toho Technical Research). The control experiment was performed in an electrochemical cell without an externally imposed electric potential. All potentials were measured against an Ag/AgCl reference electrode in saturated KCl and were converted to the SHE scale by the following equation:

$$E\ (\text{versus SHE}) = E\ (\text{versus Ag/AgCl}) + 0.198. \quad \textbf{[1]}$$

In the course of the electrolysis of solid adsorbent, the supernatant solution was sampled periodically (1 mL for each) with a stainless needle connected with a PTFE membrane filter (pore size, 0.22 μm). The filtrate was measured for pH by a portable pH meter (Seven2Go Pro, Mettler Toledo). The sample solution was also analyzed for the dissolved concentrations of ammonia and Fe^{2+} using an HPLC and an inductively coupled plasma optical emission spectrometer (ICP-OES), respectively (see below). To prevent the precipitation of Fe^{2+} via oxidation by atmospheric O_2, the solution for the ICP-OES measurement was acidified with 100 mM HCl immediately after the sampling.

After the electrolysis, the electrochemical cell was transferred immediately into an anaerobic chamber. The solid adsorbent was then separated from the supernatant solution, dried under vacuum, and stored inside the anaerobic chamber.

Analysis of Sample Solutions. The dissolved ammonium concentration was determined by postcolumn derivatization with *o*-phthalaldehyde (OPA) using a Shimadzu HPLC-fluorescence detector (FD) system. The FD was operated at 365 and 438 nm for excitation and emission, respectively. A Shim-pack WCX-1 column (4×50 mm, particle diameter = 5 μm, pore size = 300 Å) was used at 40.0 °C. A 5 mmol kg^{-1} citrate buffer solution (pH 6.2) was flowed at 1.0 mL min^{-1} for elution, and a 20 vol% methanol solution dissolving 20 mM OPA, 200 mM sodium borate, and 2 mM sodium sulfite (pH 9.2) was flowed at 0.5 mL min^{-1} for derivatization.

The dissolved Fe concentration was determined by an ICP-OES (Spectro ARCOS; AMETEK, Berwyn, PA, USA), with 1 ppm Lu as an internal standard (56). Measurements of Fe were performed using a high-matrix setup with a cross-flow nebulizer (nebulizer gas = 0.9 L min^{-1}), Scott-type standard spray chamber, and Elegra Argon humidifier. The auxiliary gas was set at 1.6 L min^{-1}.

Solid Characterization. XRD patterns of the solid adsorbents were obtained by an X-ray diffractometer (MiniFlex II, Rigaku) with Cu Kα radiation. All runs were conducted with 2θ ranging from 3° to 90°, using a 0.02° 2θ step with a scan rate of 0.01° min^{-1} for mackinawite and 0.1° min^{-1} for the other adsorbents. To prevent oxidation by atmospheric O_2 during the measurement, the samples were shielded in an air-sensitive sample holder (Rigaku) inside the anaerobic chamber. Peak identifications were made on the basis of the reference patterns reported in the Powder Diffraction File published by the International Centre for Diffraction Data.

The SSA_{BET} of solid samples were determined by a BET surface area analyzer (BELSORP mini II; MicrotracBEL, Osaka, Japan) after vacuum drying for 24 h at room temperature (23 ± 2 °C). The obtained N_2 adsorption isotherms and BET plots are shown in *SI Appendix*, Figs. S7 and S8, respectively.

Scanning electron microscopy (SEM) imaging and EDS analysis was performed on a Helios G4 UX (Thermo Fisher Scientific), equipped with an Octane Elite Super (C5) EDS detector (AMETEK) and a cryogenic stage with a preparation chamber (PP3010T, Quorum). The carbon electrode with solid sample deposited was trimmed to approximately 3×3 mm and mounted on an aluminum stub by double-sided carbon tape in an anaerobic chamber. The stub was then carried in a liquid N_2-filled plastic bag to the SEM instrument, mounted on a transfer shuttle, and inserted into the SEM stage after vacuum evacuation. To acquire surface-sensitive high-resolution images and elemental maps, an acceleration voltage of 1 kV was applied for morphological imaging, and an acceleration voltage of 5 or 20 kV for EDS analysis under a reduced pressure of $<1 \times 10^{-4}$ Pa at room temperature (23 ± 2 °C). The acceleration voltage of 20 kV was applied to average the spatial elemental distribution of mackinawite, as the characteristic X-ray is generated several μm from the point irradiated at this voltage (57).

The obtained EDS spectra were analyzed with TEAM EDS software (AMETEK). The peak intensity was converted to an atomic ratio after correction by atomic number (Z), absorption (A), and fluorescence (F). The fraction of Fe^0 against total Fe was calculated as:

$$1 - \frac{[\text{S K}]}{[\text{Fe L}]}, \quad \textbf{[2]}$$

where [S K] and [Fe L] denote the atomic concentrations calculated from the characteristic X-ray of the K line of S and that of the L line of Fe, respectively.

Nitrogen contents of solid-phase samples were measured according to the previously reported method with slight modification (58). Adsorbed nitrogen measurement was performed by an ultrasensitive elemental analyzer (FlashEA1112 series, Thermo Fisher Scientific) equipped with a narrower diameter combustion reactor (8-mm inner diameter quartz tubing, Koshin Rikagaku Seisakusho Co., Ltd., 1,050 °C), reduction reactor (8-mm inner diameter quartz tubing, Koshin Rikagaku Seisakusho Co., Ltd., 650 °C), zero-blank autosampler (Costech Analytical Technologies Inc.), and 5-mL oxygen loop

(GL Science) coupled with ConFlo IV interface and Delta plus advantage stable isotope mass spectrometer (Thermo Fisher Scientific).

X-ray absorption fine structure (XAFS) spectra at Fe K-edge were measured at BL-12C in a synchrotron radiation facility (Photon Factory) in High Energy Accelerator Research Organization (KEK). In the beamline, X-ray from a synchrotron operated at 2.5 GeV (current: 450 mA) was monochromatized with a Si(111) double-crystal monochromator, and focused to an area of 0.5×0.5 mm^2 with a bent cylindrical mirror, which also reduced the higher order. XAFS spectra were obtained in transmission mode using two ion chambers to measure intensities of incident (I_0) and transmitted (I) X-rays. The energy step within the X-ray absorption near-edge structure (XANES) region was 0.25 eV, and the absorbance by the sample (μt) was obtained as $\mu t = \ln(I/I_0)$. FeS samples were diluted with boron nitride (BN) to yield the metal/BN molar ratio of 1:25, and shielded by an O_2-impermeable polyethylene film. Measurement was conducted for a part of the sample with uniform thickness within the area of the X-ray beam.

The percentages of Fe^0 in the electrolyzed FeS were determined by a least-squares fitting of the EXAFS spectra of samples after background subtraction and normalization with XAFS data processing software ATHENA (59). The linear combination of pure FeS and pure Fe^0 was used for the fitting between 8 and 11 $Å^{-1}$. The best fit was obtained by calculating the lowest R factor, which was defined as:

$$R = \sum(\mu_{exp}(k) - \mu_{cal}(k))^2, \quad [3]$$

In this equation, μ_{exp} and μ_{cal} are the experimental and the calculated absorbances at a given wavenumber k, respectively.

First Principles Calculations. First-principles calculations were performed on a Vienna Ab-initio Simulation Package (VASP v. 5.4.4)(60), run on the Data Analyzer system in JAMSTEC. A Perdew–Burke–Ernzerhof (PBE) (61) generalized gradient approximation (GGA) exchange–correlation functional with Grimme's DFT-D3 correlation (62) was applied as a density functional, and projector augmented wave (PAW) (63) pseudopotentials were applied without consideration of spin on Fe atoms, following the literature regarding FeS calculation (64, 65). The energy cutoff was set to 450 eV. The threshold for self-consistency of the electron density was set to 10^{-5} eV, and the structural convergence threshold was set, as the forces on each ion were below 0.01 eV $Å^{-1}$. After the structural optimization of a unit cell taken from a crystallographic database (66) under Brillouin zone sampling using the Monkhorst–Pack scheme (67) with a $2\times2\times2$ k-point mesh, supercells periodic to three dimensions were created. The Brillouin zone sampling for the supercell was a $5\times5\times5$ k-point mesh for the $(2\times2\times2)$ FeS supercell and a $3\times3\times3$ k-point mesh for the $(3\times3\times3)$ and $(4\times4\times4)$ FeS supercells. The electroreduction of mackinawite to Fe^0 was expressed by the removal of one sulfur atom from the FeS supercells. NH_3 was placed at the removed sulfur position, and the atom positions and cell dimension were optimized. As for NH_3 intercalation in the pristine mackinawite, NH_3 was placed on either Fe or S, and the structure optimization was performed as described above. The intercalation energy of NH_3 (ΔE) was determined from the electron energy released through the mackinawite–NH_3 complexation,

$$\Delta E = E_{FeS-NH_3\ complex} - E_{FeS} + E_{NH_3}, \quad [4]$$

where E_X denotes the total electron energies of species X. The simulated cell dimensions are in Å, and the fractional coordinates of all the atoms involved in energy calculations are summarized in the atom coordinates section (*SI Appendix*, Tables S3–S14). Structures were displayed using VESTA v. 3.5.2 (68).

Data, Materials, and Software Availability. The authors declare that the data supporting the findings of this study are available within the paper and its *SI Appendix*.

ACKNOWLEDGMENTS. This work was supported by JSPS KAKENHI (Grant Nos. 19K04048, 19K15379, 20H00209, 21H04527, 22H05149, 22K03801, and 23K13211). We thank Shinsuke Kawagucci (JAMSTEC), Teruhiko Kashiwabara (JAMSTEC), Sakiko Kikuchi (JAMSTEC), Eiji Tasumi (JAMSTEC), Masayuki Miyazaki (JAMSTEC), and Akiko Makabe (JAMSTEC) for their technical assistance in the sample analysis. W.T. also thanks Teppei Yamada (U Tokyo), Ryuhei Nakamura (RIKEN), Hideshi Ooka (RIKEN), and Masahiro Yamamoto (JAMSTEC) for helpful discussions and insight.

Author affiliations: [a]Department of Chemistry, Graduate School of Science, The University of Tokyo, Tokyo 113-0033, Japan; [b]Institute for Extra-Cutting-Edge Science and Technology Avant-Garde Research, (X-star), Super-cutting-edge Grand and Advanced Research (SUGAR) Program, Japan Agency for Marine-Earth Science and Technology (JAMSTEC), Yokosuka 237-0061, Japan; [c]Rensselaer Astrobiology Research and Education Center, Rensselaer Polytechnic Institute, Troy, NY 12180; [d]Research Institute for Global Change, Japan Agency for Marine-Earth Science and Technology, Yokosuka 237-0061, Japan; [e]Research Institute for Marine Geodynamics, Japan Agency for Marine-Earth Science and Technology, Yokosuka 237-0061, Japan; [f]Department of Earth and Planetary Science, Graduate School of Science, The University of Tokyo, Tokyo 113-0033, Japan; and [g]Earth-Life Science Institute, Tokyo Institute of Technology, Tokyo 152-8550, Japan

Author contributions: W.T., S. Okada, and N.K. designed research; W.T. performed research; S. Okada, Y.M., S. Ono, K.T., Y.T., and N.K. contributed new reagents/analytic tools; W.T., S. Okada, Y.M., S. Ono, Y.T., and N.K. analyzed data; and N.K. wrote the paper.

1. M. J. Russell, R. M. Daniel, A. J. Hall, J. A. Sherringham, A hydrothermally precipitated catalytic iron sulphide membrane as a first step toward life. *J. Mol. Evol.* **39**, 231–243 (1994).
2. K. Takai *et al.*, Ultramafics-Hydrothermalism-Hydrogenesis-HyperSLiME (UltraH3) linkage: A key insight into early microbial ecosystem in the Archean deep-sea hydrothermal systems. *Paleontol. Res.* **10**, 269–282 (2006).
3. N. Lane, J. F. Allen, W. Martin, How did LUCA make a living? Chemiosmosis in the origin of life. *Bioessays* **32**, 271–280 (2010).
4. D. P. Summers, Ammonia formation by the reduction of nitrite/nitrate by FeS: Ammonia formation under acidic conditions. *Orig. Life Evol. Biosph.* **35**, 299–312 (2005).
5. J. A. Brandes, R. M. Hazen, H. S. Yoder Jr, Inorganic nitrogen reduction and stability under simulated hydrothermal conditions. *Astrobiology* **8**, 1113–1126 (2008).
6. S. Singireddy *et al.*, Reduction of nitrite and nitrate to ammonium on pyrite. *Orig. Life Evol. Biosph.* **42**, 275–294 (2012).
7. M. Nishizawa *et al.*, Stable abiotic production of ammonia from nitrate in Komatiite-Hosted hydrothermal systems in the Hadean and Archean oceans. *Minerals* **11**, 321 (2021).
8. H. C. B. Hansen, S. Guldberg, M. Erbs, C. Bender Koch, Kinetics of nitrate reduction by green rusts–Effects of interlayer anion and Fe(II):Fe(III) ratio. *Appl. Clay Sci.* **18**, 81–91 (2001).
9. A. Smirnov, D. Hausner, R. Laffers, D. R. Strongin, M. A. A. Schoonen, Abiotic ammonium formation in the presence of Ni–Fe metals and alloys and its implications for the Hadean nitrogen cycle. *Geochem. Trans.* **9**, 5 (2008).
10. Y. Li, A. Yamaguchi, M. Yamamoto, K. Takai, R. Nakamura, Molybdenum sulfide: A bioinspired electrocatalyst for dissimilatory ammonia synthesis with geoelectrical current. *J. Phys. Chem. C* **121**, 2154–2164 (2017).
11. Y. Li *et al.*, Enzyme mimetic active intermediates for nitrate reduction in neutral aqueous media. *Angew. Chem. Int. Ed.* **59**, 9744–9750 (2020).
12. M. L. Wong, B. D. Charnay, P. Gao, Y. L. Yung, M. J. Russell, Nitrogen oxides in early earth's atmosphere as electron acceptors for life's emergence. *Astrobiology* **17**, 975–983 (2017).
13. N. Kitadai, S. Maruyama, Origins of building blocks of life: A review. *Geosci. Front.* **9**, 1117–1153 (2018).
14. L. M. Barge *et al.*, Effects of geochemical and environmental parameters on abiotic organic chemistry driven by iron hydroxide minerals. *J. Geophys. Res. Planets* **125**, e2020JE006423 (2020).
15. D. P. Summers, S. Chang, Prebiotic ammonia from reduction of nitrite by iron (II) on the early earth. *Nature* **365**, 630–633 (1993).
16. L. P. Knauth, Temperature and salinity history of the Precambrian ocean: Implications for the course of microbial evolution. *Palaeogeogr. Palaeoclimatol. Palaeoecol.* **219**, 53–69 (2005).
17. M. P. Bernal, J. M. Lopez-Real, Natural zeolites and sepiolite as ammonium and ammonia adsorbent materials. *Bioresour. Technol.* **43**, 27–33 (1993).
18. L. Lin *et al.*, Adsorption mechanisms of high-levels of ammonium onto natural and NaCl-modified zeolites. *Sep. Purif. Technol.* **103**, 15–20 (2013).
19. A. Alshameri *et al.*, The investigation into the ammonium removal performance of Yemeni natural zeolite: Modification, ion exchange mechanism, and thermodynamics. *Powder Technol.* **258**, 20–31 (2014).
20. A. Alshameri *et al.*, Adsorption of ammonium by different natural clay minerals: Characterization, kinetics and adsorption isotherms. *Appl. Clay Sci.* **159**, 83–93 (2018).
21. H. James Cleaves *et al.*, Mineral-organic interfacial processes: Potential roles in the origins of life. *Chem. Soc. Rev.* **41**, 5502–5525 (2012).
22. M. Schoonen, A. Smirnov, C. Cohn, A perspective on the role of minerals in prebiotic synthesis. *Ambio* **33**, 539–551 (2004).
23. R. Nakamura *et al.*, Electrical current generation across a black smoker chimney. *Angew. Chem. Int. Ed.* **49**, 7692–7694 (2010).
24. M. Yamamoto *et al.*, Spontaneous and widespread electricity generation in natural Deep-Sea hydrothermal fields. *Angew. Chem. Int. Ed.* **56**, 5725–5728 (2017).
25. A. Yamaguchi *et al.*, Electrochemical CO_2 reduction by Ni-containing iron sulfides: How is CO_2 electrochemically reduced at bisulfide-bearing deep-sea hydrothermal precipitates? *Electrochim. Acta* **141**, 311–318 (2014).
26. A. Yamaguchi *et al.*, Multi-regression analysis of CO_2 electroreduction activities on metal sulfides. *J. Phys. Chem. C* **126**, 2772–2779 (2022).

27. N. Kitadai *et al*., Geoelectrochemical CO production: Implications for the autotrophic origin of life. *Sci. Adv.* **4**, eaao7265 (2018).
28. J. E. Lee *et al*., In situ FTIR study of CO_2 reduction on inorganic analogues of carbon monoxide dehydrogenase. *Chem. Commun.* **57**, 3267–3270 (2021).
29. R. Hudson *et al*., CO_2 reduction driven by a pH gradient. *Proc. Natl. Acad. Sci. U.S.A.* **117**, 22873–22879 (2020).
30. N. Kitadai *et al*., Metals likely promoted protometabolism in early ocean alkaline hydrothermal systems. *Sci. Adv.* **5**, eaav7848 (2019).
31. N. Kitadai *et al*., Thioester synthesis through geoelectrochemical CO_2 fixation on Ni sulfides. *Commun. Chem.* **4**, 37 (2021).
32. M. Wolthers, S. J. Van Der Gaast, D. Rickard, The structure of disordered mackinawite. *Am. Mineral.* **88**, 2007–2015 (2003).
33. D. W. Breck, *Zeolite Molecular Sieves: Structure, Chemistry, and Use* (John Wiley & Sons, 1973).
34. P. Kuntke *et al*., Energy-efficient ammonia recovery in an up-scaled hydrogen gas recycling electrochemical system. *ACS Sustain. Chem. Eng.* **6**, 7638–7644 (2018).
35. K. Y. Kim, D. A. Moreno-Jimenez, H. Efstathiadis, Electrochemical ammonia recovery from anaerobic centrate using a nickel-functionalized activated carbon membrane electrode. *Environ. Sci. Technol.* **55**, 7674–7680 (2021).
36. D. Hafenbradl, M. Keller, G. Wächtershäuser, K. O. Stetter, Primordial amino acids by reductive amination of α-oxo acids in conjunction with the oxidative formation of pyrite. *Tetrahedron Lett.* **36**, 5179–5182 (1995).
37. C. Huber, G. Wächtershäuser, Primordial reductive amination revisited. *Tetrahedron Lett.* **44**, 1695–1697 (2003).
38. G. S. Fonseca *et al*., Synthesis and characterization of catalytic iridium nanoparticles in imidazolium ionic liquids. *J. Colloid Interface Sci.* **301**, 193–204 (2006).
39. A. M. Beale, B. M. Weckhuysen, EXAFS as a tool to interrogate the size and shape of mono and bimetallic catalyst nanoparticles. *Phys. Chem. Chem. Phys.* **12**, 5562–5574 (2010).
40. M. Wolthers, L. Charlet, P. R. van Der Linde, D. Rickard, C. H. van Der Weijden, Surface chemistry of disordered mackinawite (FeS). *Geochim. Cosmochim. Acta* **69**, 3469–3481 (2005).
41. G. S. Otero, B. Pascucci, M. M. Branda, R. Miotto, P. G. Belelli, Evaluating the size of Fe nanoparticles for ammonia adsorption and dehydrogenation. *Comput. Mater. Sci.* **124**, 220–227 (2016).
42. S. C. Yeo, S. S. Han, H. M. Lee, Mechanistic investigation of the catalytic decomposition of ammonia (NH_3) on an Fe(100) surface: A DFT study. *J. Phys. Chem. C* **118**, 5309–5316 (2014).
43. B. Cordero *et al*., Covalent radii revisited. *Dalton Trans.* **21**, 2832–2838 (2008).
44. H. Ueda *et al*., Reactions between komatiite and CO_2-rich seawater at 250 and 350°C, 500 bars: Implications for hydrogen generation in the hadean seafloor hydrothermal system. *Prog. Earth Planet. Sci.* **3**, 35 (2016).
45. T. Nunoura *et al*., A primordial and reversible TCA cycle in a facultatively chemolithoautotrophic thermophile. *Science* **359**, 559–563 (2018).
46. Y. Sekine *et al*., High-temperature water-rock interactions and hydrothermal environments in the chondrite-like core of Enceladus. *Nat. Commun.* **6**, 8604 (2015).
47. P. L. Morrill *et al*., Geochemistry and geobiology of a present-day serpentinization site in California: The cedars. *Geochim. Cosmochim. Acta* **109**, 222–240 (2013).
48. E. S. Boyd, M. J. Amenabar, S. Poudel, A. S. Templeton, Bioenergetic constraints on the origin of autotrophic metabolism. *Philos. Trans. A Math. Phys. Eng. Sci.* **378**, 20190151 (2020).
49. D. S. Kelley *et al*., An off-axis hydrothermal vent field near the mid-Atlantic ridge at 30°N. *Nature* **412**, 145–149 (2001).
50. H. Song *et al*., The onset of widespread marine red beds and the evolution of ferruginous oceans. *Nat. Commun.* **8**, 399 (2017).
51. T. Shibuya, M. J. Russell, K. Takai, Free energy distribution and hydrothermal mineral precipitation in Hadean submarine alkaline vent systems: Importance of iron redox reactions under anoxic conditions. *Geochim. Cosmochim. Acta* **175**, 1–19 (2016).
52. A. W. Lounsbury *et al*., Preferential adsorption of selenium oxyanions onto 110 and 012 nano-hematite facets. *J. Colloid Interface Sci.* **537**, 465–474 (2019).
53. M. Zhu, Y. Wang, D. Meng, X. Qin, G. Diao, Hydrothermal synthesis of hematite nanoparticles and their electrochemical properties. *J. Phys. Chem. C* **116**, 16276–16285 (2012).
54. Y. S. Kang, S. Risbud, J. F. Rabolt, P. Stroeve, Synthesis and characterization of nanometer-size Fe_3O_4 and γ-Fe_2O_3 particles. *Chem. Mater.* **8**, 2209–2211 (1996).
55. N. Kitadai, K. Nishiuchi, W. Takahagi, Thermodynamic impact of mineral surfaces on amino acid polymerization: Aspartate dimerization on two-line ferrihydrite, anatase, and γ-alumina. *Minerals* **11**, 234 (2021).
56. M. Grotti, E. Magi, R. Leardi, Selection of internal standards in inductively coupled plasma atomic emission spectrometry by principal component analysis. *J. Anal. At. Spectrom.* **18**, 274–281 (2003).
57. T. Sakurada *et al*., Lateral resolution of EDX analysis with ultra low acceleration voltage SEM. *J. Surf. Anal.* **12**, 118–121 (2005).
58. N. Ogawa, T. Nagata, H. Kitazato, N. Ohkouchi, "Ultra-sensitive elemental analyzer/isotope ratio mass spectrometer for stable nitrogen and carbon isotope analyses" in *Earth, Life and Isotopes*, N. Ohkouch, I. Tayasu, K. Koba, Eds. (Kyoto University Press, 2010), pp. 339–353.
59. B. Ravel, M. Newville, ATHENA, ARTEMIS, HEPHAESTUS: Data analysis for X-ray absorption spectroscopy using IFEFFIT. *J. Synchrotron Radiat.* **12**, 537–541 (2005).
60. G. Kresse, J. Furthmüller, Efficient iterative schemes for ab initio total-energy calculations using a plane-wave basis set. *Phys. Rev. B Condens. Matter* **54**, 11169–11186 (1996).
61. J. P. Perdew, K. Burke, M. Ernzerhof, Generalized gradient approximation made simple. *Phys. Rev. Lett.* **77**, 3865–3868 (1996).
62. S. Grimme, J. Antony, S. Ehrlich, H. Krieg, A consistent and accurate ab initio parametrization of density functional dispersion correction (DFT-D) for the 94 elements H-Pu. *J. Chem. Phys.* **132**, 154104 (2010).
63. F. Jollet, M. Torrent, N. Holzwarth, Generation of projector augmented-Wave atomic data: A 71 element validated table in the XML format. *Comput. Phys. Commun.* **185**, 1246–1254 (2014).
64. N. Y. Dzade, A. Roldan, N. H. de Leeuw, Adsorption of methylamine on mackinawite (FeS) surfaces: A density functional theory study. *J. Chem. Phys.* **139**, 124708 (2013).
65. N. Y. Dzade, N. H. de Leeuw, Adsorption and desulfurization mechanism of thiophene on layered FeS(001), (011), and (111) surfaces: A dispersion-corrected density functional theory study. *J. Phys. Chem. C, Nanomater. Interfaces* **122**, 359–370 (2018).
66. A. R. Lennie, S. A. T. Redfern, P. F. Schofield, D. J. Vaughan, Synthesis and Rietveld crystal structure refinement of mackinawite, tetragonal FeS. *Mineral. Mag.* **59**, 677–683 (1995).
67. H. J. Monkhorst, J. D. Pack, Special points for Brillouin-zone integrations. *Phys. Rev. B, Condens. Matter* **13**, 5188–5192 (1976).
68. K. Momma, F. Izumi, VESTA 3 for three-dimensional visualization of crystal, volumetric and morphology data. *J. Appl. Crystallogr.* **44**, 1272–1276 (2011).